



# The effect of slip distribution on flow past a circular cylinder



Dandan Li<sup>a</sup>, Shichen Li<sup>a</sup>, Yahui Xue<sup>a</sup>, Yantao Yang<sup>a</sup>, Weidong Su<sup>a</sup>,  
Zhenhua Xia<sup>a</sup>, Yipeng Shi<sup>a</sup>, Hao Lin<sup>b,\*</sup>, Huiling Duan<sup>a,c,d,\*\*</sup>

<sup>a</sup> State Key Laboratory for Turbulence and Complex Systems, Department of Mechanics and Engineering Science, College of Engineering, Peking University, Beijing 100871, China

<sup>b</sup> Mechanical and Aerospace Engineering Department, Rutgers, The State University of New Jersey, 98 Brett Rd, Piscataway, New Jersey 08854, USA

<sup>c</sup> Key Laboratory of High Energy Density Physics Simulation, Center for Applied Physics and Technology, Peking University, Beijing 100871, China

<sup>d</sup> State Key Laboratory of Nonlinear Mechanics (LNM), Institute of Mechanics, Chinese Academy of Science, Beijing 100190, China

## ARTICLE INFO

### Article history:

Received 21 March 2014

Accepted 27 August 2014

Available online 30 October 2014

### Keywords:

Slip boundary  
Circular cylinder  
Drag reduction

## ABSTRACT

A slip boundary has been shown to have a significant impact on flow past bluff bodies. In this work and using a circular cylinder as a model system, the effects of various slip configurations on the passing flow are investigated. A theoretical analysis using matched-asymptotic expansion is first performed in the small-Reynolds number regime following Stokes and Oseen. A slip boundary condition is shown to lead to only higher-order effects ( $\sim 1/\ln(\text{Re})$ ) on the resulting drag coefficient. For higher Reynolds numbers (100–500), the effects of five types of symmetric slip boundary conditions, namely, no slip, fore-side slip, aft-side slip, flank slip, and all slip on the flow field and pertinent parameters are investigated with numerical simulations. Detailed results on the flow structure and force distribution are presented. Flank slip is found to have the best effect for drag reduction with comparable coverage of slip area. For asymmetric slip distributions, torque and lift are found to generally occur.

© 2014 Elsevier Ltd. All rights reserved.

## 1. Introduction

The flow past a circular cylinder is a classical example of flow past a bluff body. This phenomenon, first examined in an experimental study by Strouhal in 1878 (Strouhal, 1878), often serves as a benchmark to help understand flow separation and vortex shedding, which are closely related to increased drag and root mean square lift, and structural vibrations. Extensive research has been performed on this classical problem in the past century. Based on the Oseen equation, Lamb obtained a solution for a slow, steady, viscous, and incompressible flow (Lamb, 1911). Several more advanced methods were developed subsequently to improve flow prediction. Lagerstrom and Cole introduced Stokes and Oseen variables so as to obtain Stokes and Oseen expansions in 1955 (Lagerstrom and Cole, 1955). Proudman and Pearson advanced the solution to high-order approximations in 1957 (Proudman and Pearson, 1957). The solution based on the Stokes and Oseen equations offers an analytical description of the flow field and pertinent parameters such as the drag, pressure, and lift coefficients.

\* Corresponding author.

\*\* Corresponding author.

E-mail addresses: [hlin@jove.rutgers.edu](mailto:hlin@jove.rutgers.edu) (H. Lin), [hlduan@pku.edu.cn](mailto:hlduan@pku.edu.cn) (H. Duan).

As a simple and classic model, flow past a circular cylinder has always been used to explore means of flow control around a bluff body. Flow control includes both passive and active techniques to impart desired change on the flow field (Fish and Lauder, 2006; Choi et al., 1994), (Sirovich and Karlsson). Passive control methods are in general easier to implement when compared with active methods, and include, for example, geometric shaping to manipulate the pressure gradient, the use of fixed mechanical vortex generators and splitters for separation control (Ozono, 1999), and the placement of directional grooves or riblets on a surface to create effective slip for drag reduction (Rothstein, 2010) and change of the flow field (Ou et al., 2007). Following this approach, we focus on the passive methods, and explore the effects of slip boundaries on flow, drag and lift.

A slip boundary is usually characterized by a slip length which is the fictitious distance between the physical interface and an imaginary surface inside the body where the tangential velocity is zero. In most continuum studies (Hanchi et al., 1999; Breuer, 2000), the Navier-Stokes equations are employed in conjunction with no-slip boundary conditions. However, the violation of this condition is possible, in particular on the micro- and nano-scales, and on hydrophobic surfaces (Lauga et al., 2007). For example, Joseph et al. directly measured the apparent slip length on hydrophobic surfaces in flow through thin micro channels (Joseph and Tabeling, 2005). Large slip lengths up to 400  $\mu\text{m}$  can be realized by using super-hydrophobic surfaces, on which the liquid is mostly in contact with air that trapped in the structured or unstructured crevices of the engineered surfaces (Qu  r  , 2005; Lee and Kim, 2009; Xue et al., 2012). Due to the low viscosity of air, fluid flow over the air-water interface is nearly shear-free, leading to overall drag reduction. This “apparent” slip effect can be further enhanced if a coherent air layer can be formed on the object surface (Vakarelski et al., 2012), which leads to very large effective slip length. For these cases, the no-slip boundary condition may actually hold on the microscopic level, and the slip is only an apparent phenomenon on the macroscopic perspective due to presence of various fractions of air-liquid interfaces. Priezjev et al. numerically studied the effective slip behavior on substrates with alternating shear-free and no-slip boundary conditions under shear flow in micro channels with both continuum and molecular dynamics simulations (Priezjev et al., 2005). Lund and co-authors obtained expressions for an effective slip boundary condition in certain cases, which they then extended to surfaces with periodic roughness (Hendy and Lund, 2007; Lund et al., 2012). With molecular dynamics simulations, Thalakkottor and Mohseni investigated slip in unsteady flows, and found that it was governed by both the shear rate and its temporal gradient (Thalakkottor and Mohseni, 2013). Muralidhar et al. experimentally investigated the effects of an induced slip on the behavior of flow around super-hydrophobic cylinders (Muralidhar et al., 2011). The presence of slip was found to notably impact the vortex shedding dynamics in the wake of the cylinder (Daniello et al., 2013). Legendre et al. numerically studied the flow past circular cylinders with slip uniformly distributed on the surface (Legendre et al., 2009), and showed that drag reduction increased for a given Reynolds number, and that the onset of vortex shedding was delayed with increasing slip length. Another numerical study investigated the effects of alternating circumferential bands of slip and no-slip (You and Moin, 2007). The bands were periodically distributed with different arc lengths that are on the order of the cylinder diameter, and the slip length was 2% of the cylinder diameter in both streamwise and spanwise directions. The results showed that the drag and root mean square lift decreased by as much as 75%. Swan and Khair investigated the hydrodynamics of a micro-scale spherical particle in a low Reynolds number flow, and found that the motion of the particle can be changed by a slip-stick boundary on the particle surface (Swan and Khair, 2008). Together, these studies suggest that implementing slip is an effective means to achieve flow control and desired effects such as drag reduction.

In this work, we follow these previous efforts, and present a comprehensive study of flow past a circular cylinder with slip boundaries. We first investigate the regime of small Reynolds numbers. In this regime, an analytical solution using the method of matched asymptotic expansion following Stokes and Oseen is attainable. For laminar flow with moderate-to-large Reynolds numbers (100–500), we implement numerical simulations, and investigate five types of slip distributions, namely, no slip, fore-side slip, aft-side slip, flank slip, and all slip. We discuss how these different geometric configurations can impact the flow field, wake dynamics, vortex shedding, and drag and lift coefficients. We are motivated to provide guidance to the strategic planning of slip boundary placement on a bluff body for desired flow control.

This paper is organized as follows. Problem formulation and numerical methods are described in Section 2. The analytic solution in the small-Reynolds-number limit is presented and discussed in Section 3. Numerical simulation of flows with various types of slip distributions is presented in Section 4. In Section 5 we draw conclusions.

## 2. Problem formulation and numerical methods

### 2.1. Governing equations and boundary conditions

For a two-dimensional, viscous, and incompressible flow, the governing equations for velocity  $\mathbf{u}$  and pressure  $p$  are:

$$\frac{\partial \mathbf{u}}{\partial t} + \mathbf{u} \cdot \nabla \mathbf{u} = -\frac{1}{\rho} \nabla p + \frac{2\mu}{\rho} \nabla \cdot \mathbf{S}, \quad \nabla \cdot \mathbf{u} = 0, \quad (1)$$

where  $\rho$  is the fluid density,  $\mu$  is dynamic viscosity, and  $\mathbf{S} = (\nabla \mathbf{u} + (\nabla \mathbf{u})^T)/2$  is the rate-of-strain tensor. The surface satisfies the impermeability and slip boundary conditions (Legendre et al., 2009),

$$\begin{aligned} \mathbf{n} \cdot \mathbf{u} &= 0, \\ \mathbf{n} \times \mathbf{u} &= 2L_s \mathbf{n} \times (\mathbf{S} \cdot \mathbf{n}). \end{aligned} \quad (2)$$

where  $\mathbf{n}$  is the unit normal vector, and  $L_s$  is the slip length. Three dimensionless parameters are involved in this study: the Reynolds number,  $Re = \rho U D / \mu$ ; the nondimensionalized slip length,  $\beta = L_s / D$ ; and the Strouhal number,  $St = f D / U$ . Here  $U$  is the fluid velocity in the far field,  $D$  is the diameter of the cylinder,  $L_s$  is the slip length, and  $f$  is the frequency of vortex shedding. We will also use the following definitions: the pressure coefficient,  $C_p = \frac{p - p_\infty}{\frac{1}{2} \rho U^2}$ ; the drag coefficient  $C_D = \frac{F_D}{\frac{1}{2} \rho U^2 A}$ ; the r.m.s. lift coefficient,  $C_L = \frac{F_L}{\frac{1}{2} \rho U^2 A}$ ; the mean lift coefficient,  $C_{LM} = \frac{F_{LM}}{\frac{1}{2} \rho U^2 A}$ ; the torque coefficient,  $C_T = \frac{T}{\frac{1}{2} \rho U^2 A D}$ . Here  $F_D$  is the time-averaged drag acting on the surface,  $F_L$  is the time-averaged root-mean-square lift,  $F_{LM}$  is the time-averaged lift,  $T$  is the time-averaged torque acting on the cylinder,  $A$  is the intercept area of the cylinder, and  $p_\infty$  is the ambient pressure.

## 2.2. Numerical methods

Numerical simulation is performed using the commercial software FLUENT 6.1 (Fluent Inc., Lebanon, NH). This software has been proven to perform with high accuracy on similar fluid mechanical problems. Examples include Taylor vortex flow (Deng et al., 2006), flow past a static or rotating circular cylinder (Gillies, 1998; Padrino and Joseph, 2006), flow past a cylinder close to a free surface (Reichl et al., 2005), and laminar flow on structured surfaces (Ou et al., 2007). The numerical results are often validated, e.g., with experimental measurements (Gillies, 1998) and alternative simulation methods (Mittal and Kumar, 2003). For the present study, a Semi-Implicit Method for Pressure-Linked Equation, or SIMPLE-based algorithm is chosen to solve Eqs. (1, 2) (Patankar, 1980). Briefly speaking, the momentum equation is first solved with a “guessed” pressure field. The Poisson equation is then solved to compute the pressure correction at the new iteration step. The velocity field is subsequently updated with corrected pressure. This process repeats until the divergence-free condition is met with satisfactory accuracy. The algorithm is second-order in general. We refer interested readers to the User’s Guide for further details (Fluent 6.1). We use two types of grids. The first type is used for the validation of the analytical solution in Section 3,

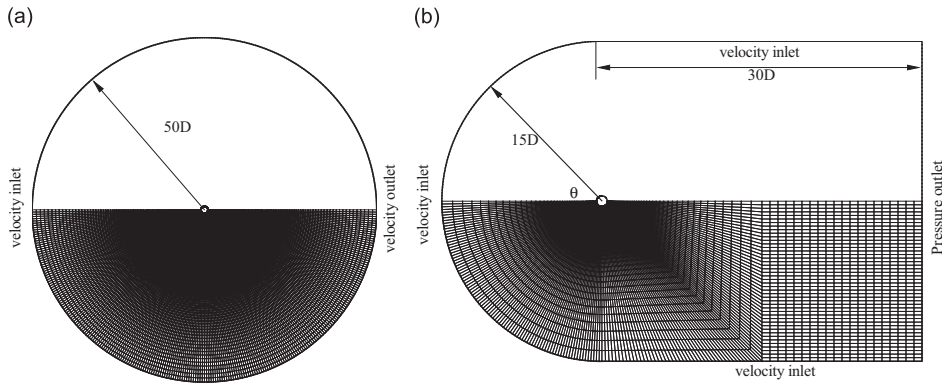


**Fig. 1.** The two-dimensional computational domain and grids. (a) The computational domain for the validation of the analytical solution in Section 3. (b) The computational domain for the study of the effects of distributed slip in Section 4. For both cases,  $(r, \theta)$  denote the cylindrical coordinate system, and  $D$  is the diameter of the cylinder.

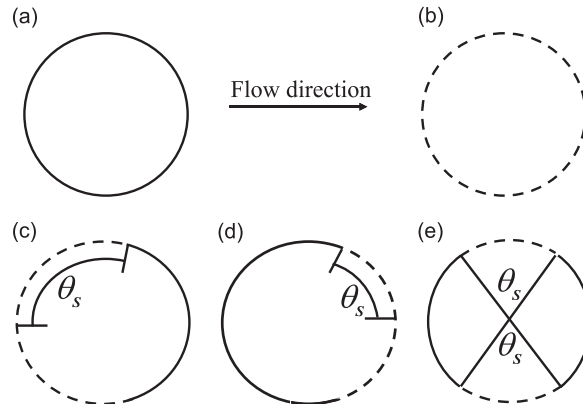


**Fig. 2.** Diagram of five slip boundary distributions (spanwise distributed): (a) no slip; (b) all slip; (c) fore-side slip; (d) aft-side slip; (e) flank slip. Black solid line denotes no slip; dashed, slip on the cylindrical surface. The slip span is denoted by  $\theta_s$ , half of the total azimuth which is symmetric about the center axis along the flow direction.

and is shown in Fig. 1a. The boundary of the computational zone satisfies the Oseen solution in the far field, and a big circular computational domain facilitates this implementation. The cylinder surface satisfies the slip boundary condition (2). The computational domain has a radius of  $50D$ , where  $D$  is the diameter of the cylinder. The total number of grid points is 43,200, and the thickness of the first row of cells next to the cylindrical surface is  $0.001D$ . The second type is used for the study of the effects of distributed slip in Section 4 and shown in Fig. 1b. The computational domain includes two blocks which are semicircular and rectangular, respectively. The inclusion of the rectangular block is to facilitate capturing of vortex shedding, e.g., as seen in Fig. 5 below. The left, top and bottom boundaries of the computational domain are the velocity inlets. The incoming flow is uniform. Equation (2) is similarly prescribed on the cylindrical surface. The right boundary of the computational domain is a pressure outlet. The total number of grid points is 30,000, and the thickness of the first row of cells next to the cylindrical surface is  $0.004D$ . Results on numerical convergence and accuracy are presented in Appendix A.

Fig. 2 shows five types of slip distribution considered: (a) no slip; (b) all slip; (c) fore-side slip; (d) aft-side slip; (e) flank slip. For all cases, the slip boundary is symmetrically distributed about the center axis along the flow direction. The span of the slip is denoted by the half-azimuth,  $\theta_s$ .

### 3. Analytic solution at low Reynolds numbers

In this section, we first obtain an analytical solution for flow past a cylinder with a slip interface in the small-Reynolds number limit. Our analysis follows closely that by Proudman and Pearson (Proudman and Pearson, 1957). Briefly speaking, the stream function is expanded to Stokes and Oseen expansions, respectively, with the slip boundary condition for the Stokes expansion, and a uniform-stream condition for the Oseen expansion. The two expansions are both derived from the same exact solution leading to a matching procedure yielding further constraints. For steady-state incompressible flow, the dimensionless form of the governing equations can be written as

$$\begin{cases} -\nabla p + \nabla^2 \mathbf{u} = \text{Re}_a \mathbf{u} \cdot \nabla \mathbf{u}, \\ \nabla \cdot \mathbf{u} = 0, \end{cases} \quad (3)$$

where  $\text{Re}_a = \rho Ua/\mu$ , and  $a$  is the radius of the cylinder. Similarly, Eq. (2) assumes the following form in a cylindrical coordinate

$$\begin{cases} u_r|_{r=1} = 0, \\ u_\theta|_{r=1} = \frac{\beta}{1+\beta} \frac{\partial u_\theta}{\partial r}|_{r=1}. \end{cases} \quad (4)$$

In the far-field, the boundary conditions are

$$\begin{cases} u_r|_{r \rightarrow \infty} = \cos \theta, \\ u_\theta|_{r \rightarrow \infty} = -\sin \theta. \end{cases} \quad (5)$$

Equations (3–5) can be re-written in terms of a dimensionless stream function,  $\phi$

$$\nabla_r^4 \phi = -\frac{\text{Re}_a}{r} \frac{\partial(\phi, \nabla^2 \phi)}{\partial(r, \theta)}. \quad (6)$$

$$\begin{cases} \frac{\partial \phi}{\partial \theta}|_{r=1} = 0, \\ \frac{\partial \phi}{\partial r}|_{r=1} = \frac{\beta}{1+\beta} \frac{\partial^2 \phi}{\partial r^2}|_{r=1}, \end{cases} \quad (7)$$

$$\phi|_{r \rightarrow \infty} = r \sin \theta. \quad (8)$$

We use Stokes and Oseen expansions to search an approximate solution following Proudman and Pearson (Proudman and Pearson, 1957). More details about these expansions are found in Lagerstrom and Cole (Lagerstrom and Cole, 1955). We define the Stokes variables:  $(r, \theta, \phi)$  and  $(\sigma, \theta, \psi)$ , where  $(r, \theta)$  are the polar coordinates,  $\sigma = \text{Re}_a r$ , and  $\psi = \text{Re}_a \phi$ . The Stokes and Oseen stream functions, denoted by  $\phi$  and  $\psi$ , respectively, are then expanded in terms of the Reynolds number

$$\begin{aligned} \phi(r, \theta) &= f_0(\text{Re}_a)\phi_0(r, \theta) + f_1(\text{Re}_a)\phi_1(r, \theta) + \cdots + f_n(\text{Re}_a)\phi_n(r, \theta) + \cdots, \\ \lim_{\text{Re}_a \rightarrow 0} \frac{f_{n+1}(\text{Re}_a)}{f_n(\text{Re}_a)} &= 0. \end{aligned} \quad (9)$$

$$\begin{aligned} \psi(\sigma, \theta) &= F_0(\text{Re}_a)\psi_0(\sigma, \theta) + F_1(\text{Re}_a)\psi_1(\sigma, \theta) + \cdots + F_n(\text{Re}_a)\psi_n(\sigma, \theta) + \cdots, \\ \lim_{\text{Re}_a \rightarrow 0} \frac{F_{n+1}(\text{Re}_a)}{F_n(\text{Re}_a)} &= 0. \end{aligned} \quad (10)$$

where  $f$  and  $F$  are functions of  $\text{Re}$ . The leading term of the Stokes expansion satisfies Stokes approximation, and that of the Oseen expansion satisfies Oseen approximation. We search for two solutions: one is in the form of the Stokes expansion  $\phi$  near the cylindrical surface, and satisfies Eq. (9) on the surface; the other is in the form of the Oseen expansion  $\psi$ , and

satisfies Eq. (10) in the far-field. These two solutions are subsequently matched where both are valid. Proudman and Pearson (Proudman and Pearson, 1957) obtained a solution by considering  $f_n(\text{Re}_a) = F_n(\text{Re}_a) = (1/\ln \text{Re}_a)^n$  in case of a no-slip boundary condition on the surface of the cylinder. The solution in the vicinity of the cylinder is

$$\phi = - \left[ \frac{1}{\ln \text{Re}_a} + \frac{\frac{1}{2} - \gamma + \ln 4}{\ln^2 \text{Re}_a} \right] \left[ r \ln r + \frac{1}{2} \left( \frac{1}{r} - r \right) \right] \sin \theta, \quad (11)$$

where  $\gamma$  is Euler's constant. Our solution assumes a similar form:

$$\phi = - \left[ \frac{1}{\ln \text{Re}_a} + \frac{1 - \frac{1}{2(1+2\beta)} - \gamma + \ln 4}{\ln^2 \text{Re}_a} \right] \left[ r \ln r + \frac{1}{2(1+2\beta)} \left( \frac{1}{r} - r \right) \right] \sin \theta. \quad (12)$$

We observe that the only difference is that the factor of  $1/2$  is replaced by  $1-1/[2(1+2\beta)]$  in Eq. (12). Alternatively, Kaplun obtained a solution where the asymptotic expansion was performed in terms of powers of  $\varepsilon$ , where  $\varepsilon^{-1} = \ln(4/\text{Re}_a) - 1/2 + \gamma$  (Kaplun, 1957). He obtained the drag coefficient as  $C_D = 4\pi\mu U(\varepsilon - 0.87\varepsilon^3)$ , the leading order of which corroborates with Lamb's result (Lamb, 1911) with an Oseen equation. Comparisons with experimental results reveal that this form of solution is more accurate when compared with that provided by Eq. (11). For this reason, we elect to present our solution in a form following Kaplun (Kaplun, 1957)

$$\phi = - \frac{1}{\Delta(\text{Re}_a)} \left[ r \ln r + \frac{1}{2(1+2\beta)} \left( \frac{1}{r} - r \right) \right] \sin \theta, \quad (13)$$

where  $1/\Delta(\text{Re}_a) = 1/\{ \ln \text{Re}_a - [1 - 1/(2+4\beta) - \gamma + \ln 4] \}$ . Note that Eqs. (12) and (13) are consistent up to  $O(1/\ln^2(\text{Re}_a))$ . More details of the derivation are found in Appendix B. Here we simply present the final result of interest, namely, the drag coefficient:

$$C_D = \left[ \frac{1}{1 - \frac{1}{2(1+2\beta)} - \gamma - \ln(\text{Re}_a/4)} \right] \frac{4\pi}{\text{Re}_a}. \quad (14)$$

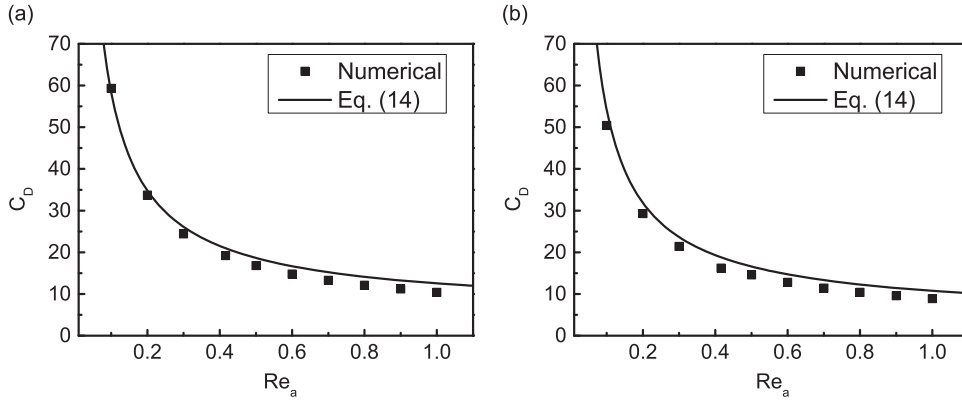


Fig. 3. Comparison of  $C_D$  from Eq. (14) and numerical simulation. (a)  $\beta=0$ ; (b)  $\beta=1$ .

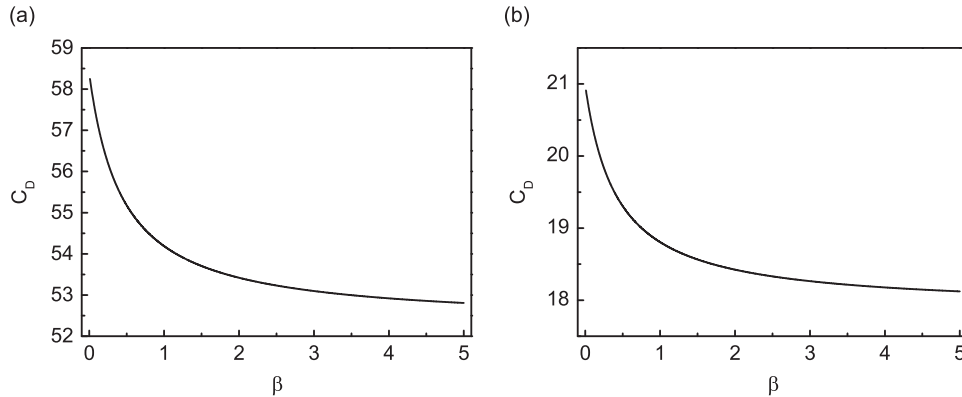


Fig. 4. The drag coefficient,  $C_D$ , as a function of  $\beta$  for two Reynolds numbers: (a)  $\text{Re}_a=0.1$ ; (b)  $\text{Re}_a=0.416$ .



For  $\beta=0$ , Eq. (14) recovers the result by Lamb where there is no slip present (Lamb, 1911). For validation of this approximate solution, we compare the drag coefficient predicted by Eq. (14) as a function of the Reynolds number for  $\beta=0$  and 1 with numerical simulation. The results are shown in Fig. 3. Good agreements are found between the two. The difference is negligible for  $Re_a < 0.2$ . For  $0.2 < Re_a < 1$ , the difference is less than 10%.

Equation (14) provides an analytical expression based on which we can assess the effects of slip on drag reduction. In fact, it explicitly states that slip causes only higher order modifications to the drag coefficient. Fig. 4 shows  $C_D$  as a function of  $\beta$  for two typical Reynolds numbers, namely, 0.1 and 0.416. In Eq. (14), the boundary condition only enters the expression for stream function on the second-order expansion in terms of  $1/\ln(Re_a)$ . (For a small Reynolds number,  $1/\ln(Re_a)$  is also a small number.) Consequently, in Eq. (14), in the denominator of the first multiplying factor,  $\ln(Re_a)$  dominates over  $1/[2(1+2\beta)]$ . For this reason, the drag coefficient is not sensitive to the boundary condition on the cylindrical surface, be it slip or no slip. The general conclusion of this section is therefore that slip is not an effective means for flow control in the limit of small Reynolds numbers.

#### 4. Numerical simulation of distributed slip boundaries

For moderate Reynolds numbers, an analytical solution is in general not attainable, and numerical simulation is used instead to explore the effects of slip on flow past a cylinder. In what follows, we first examine in detail one type of slip distribution, namely, fore-side slip. The flow field and pertinent parameters are studied as functions of both the slip span  $\theta_s$ , and the Reynolds numbers. A comparison of all five types of slip distribution then follows. For all cases, we set  $\beta=0.2$ .

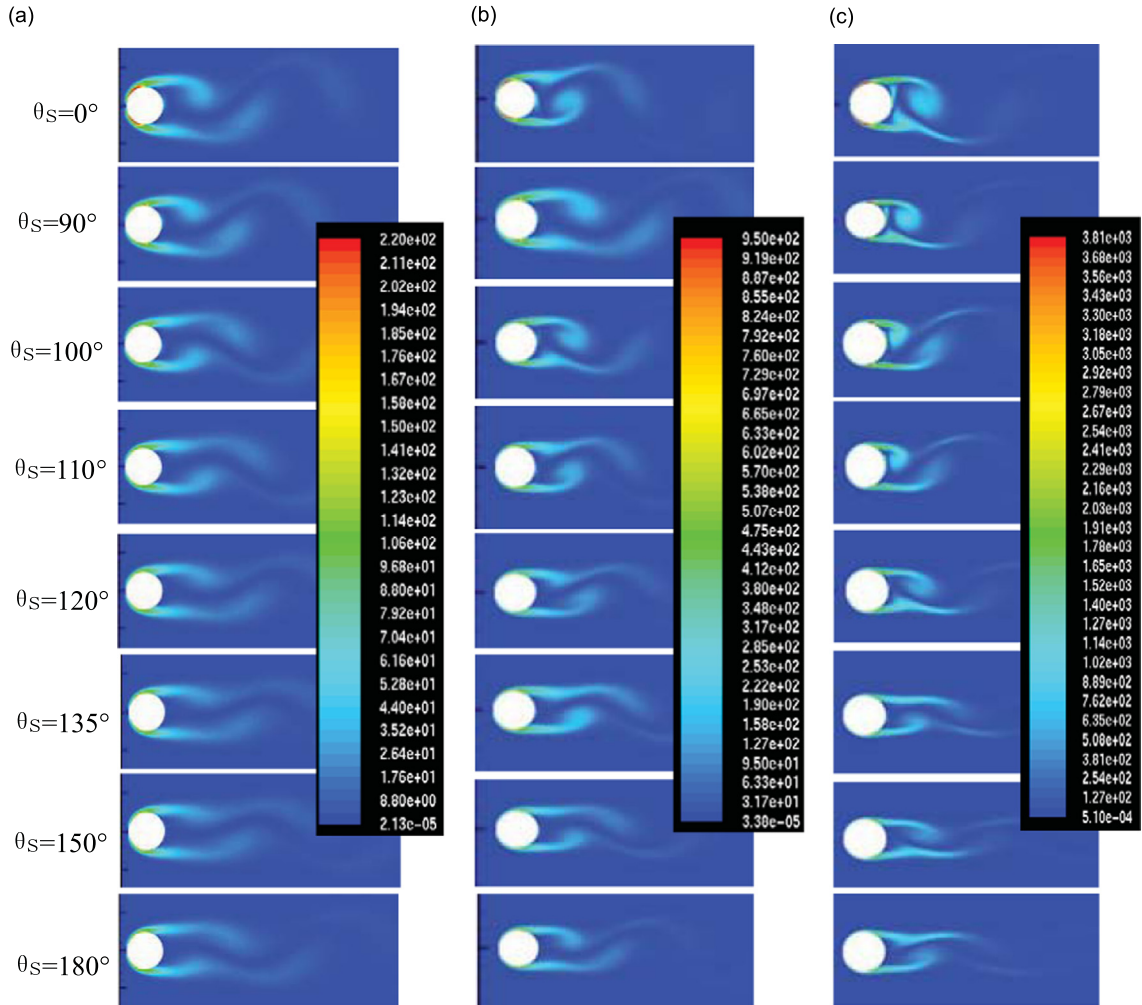


**Fig. 5.** Contour plot of vorticity at  $t=50$  s with fore-side slip: (a)  $Re=100$ ; (b)  $Re=200$ ; (c)  $Re=500$ . The color map is the same for each Reynolds number, and the unit is  $s^{-1}$ . For all cases  $\beta=0.2$ .

#### 4.1. Simulation with fore side slip distribution

Fig. 5 shows the instantaneous vorticity distribution at  $t=50$  s for three typical Reynolds numbers,  $Re=100$ , 200 and 500. For fore-side slip distribution,  $\theta_s=0^\circ$  and  $180^\circ$  are equivalent to no slip and all slip, respectively, which serve as references for comparison. We observe that as  $\theta_s$  increases, vorticity on the wall decreases overall. Most notably, the wake region narrows and becomes more stable. This result correlates with the recession of the time-averaged separation angle,  $\theta_{sep}$ , which is shown in Fig. 6. Note that for  $\theta_s=0^\circ$ , our simulation gives  $\theta_{sep}=116^\circ$  and  $110^\circ$  for  $Re=100$  and 200, respectively, in close agreement with the experimental measurement of  $114^\circ$  and  $106^\circ$  from Wu et al. (2004). For all Reynolds numbers presented (100, 200, and 500), the separation angle gradually increases until a plateau is reached at around  $\theta_s=150^\circ$ .

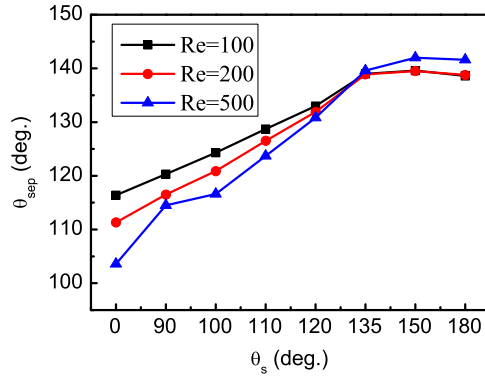


Fig. 6. The time-averaged separation angle,  $\theta_{sep}$ , as a function of  $\theta_s$  for fore-side slip distribution. For all cases  $\beta=0.2$ .

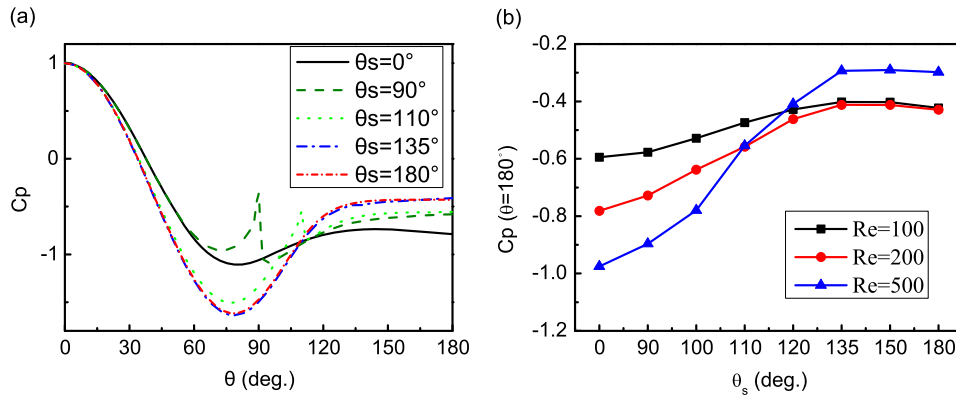


Fig. 7. (a) The pressure coefficient on the wall of the cylinder for  $\beta=0.2$  and  $Re=200$ ; (b) The pressure coefficient at  $\theta=180^\circ$  as a function of  $\theta_s$  for  $\beta=0.2$ .

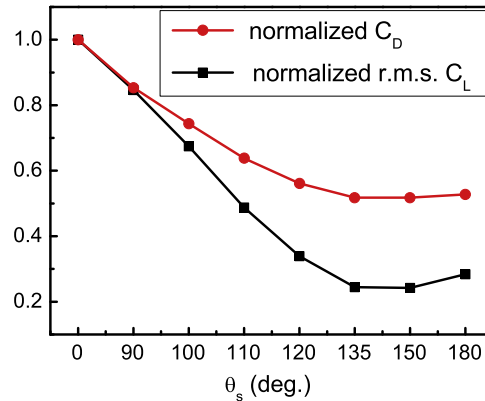
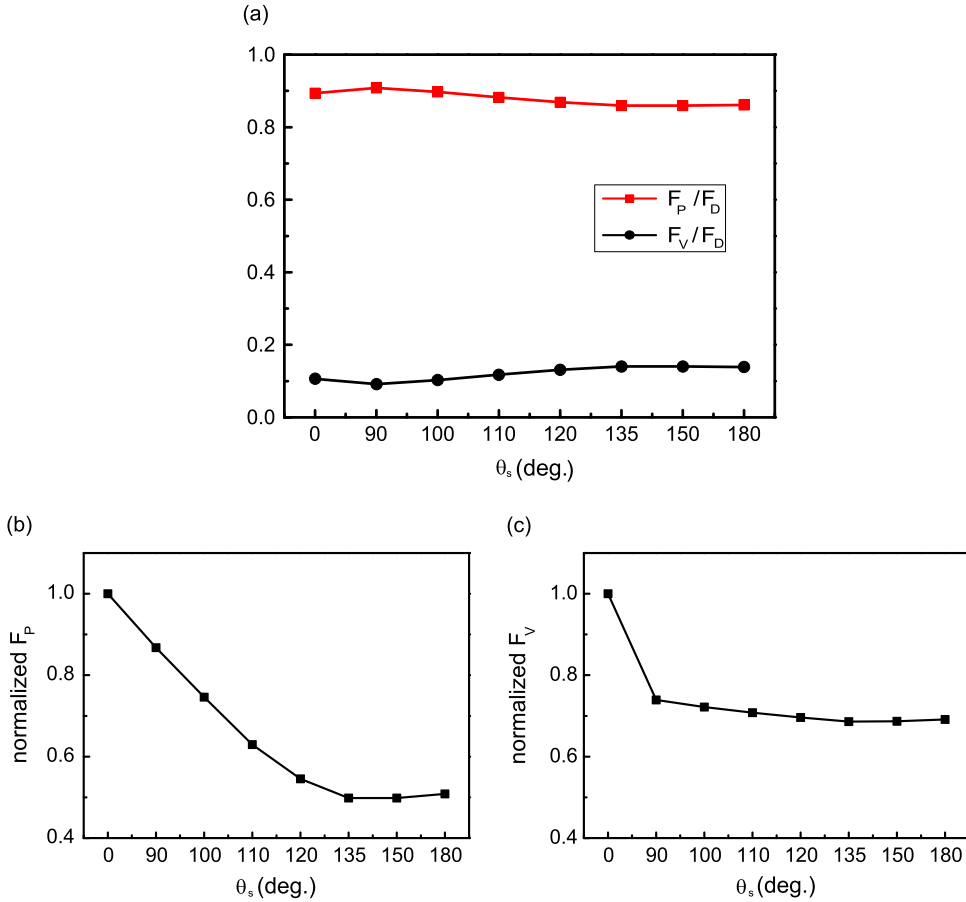
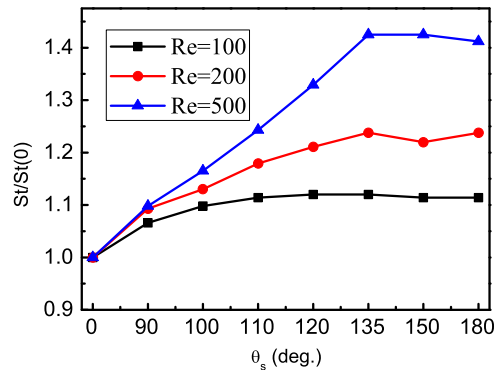


Fig. 8. The normalized drag coefficient and r.m.s. lift coefficient as functions of  $\theta_s$  for fore-side slip. Here  $Re=200$  and  $\beta=0.2$ .

The recession of wake region and separation locale is closely related to the pressure distribution on the cylinder wall. Fig. 7a shows the pressure coefficient as a function of  $\theta$  for various slip azimuth,  $\theta_s$ . Here,  $\theta_s = 0^\circ$  corresponds to no slip, and has the lowest pressure in the wake. The fore-aft pressure difference is the main contributor of drag on the body (see also Fig. 9 below). For  $\theta_s = 180^\circ$  (all slip) the wake pressure is the highest, leading to the most drag reduction. This result corroborates with those by Legendre et al. (2009). For partial fore-side slip with  $\theta_s$  between  $0^\circ$  and  $180^\circ$ , the behavior of  $C_p$  is peculiar. First, a peak occurs at the interface between slip and no slip, namely,  $\theta = \theta_s$ . This result is not surprising, as the fluid velocity near the wall experiences a sudden decrease near this transitional region. The peak becomes less conspicuous as  $\theta_s$  increases. Second, the wake pressure increases along with  $\theta_s$ . Fig. 7b shows the pressure coefficient at  $\theta = 180^\circ$  for



**Fig. 9.** Behavior of contributors to total drag.  $F_p$  is the force due to pressure difference, and  $F_v$  is skin friction.  $F_D$  is total drag. For (b) and (c),  $F_p$  and  $F_v$  are normalized with their respective values at  $\theta_s = 0^\circ$  (no slip).  $Re=200$  and  $\beta=0.2$ .



**Fig. 10.** The Strouhal number as a function of  $\theta_s$ . Normalization for each Reynolds number is performed with the respective values at  $\theta_s = 0^\circ$ .  $\beta=0.2$ .



three Reynolds numbers (100, 200, and 500). As  $\theta_s$  increases,  $C_p$  also increases, until a plateau is reached at around  $\theta_s = 135^\circ$ . This plateau corroborates with that in the separation angle shown in Fig. 6.

Next we examine the behavior of drag and lift coefficients. In Fig. 8, both  $C_D$  and the r.m.s.  $C_L$  are normalized by their respective values at  $\theta_s = 0^\circ$  (no slip). Both coefficients decrease along with an increase in  $\theta_s$ , and the reduction effects saturate at  $\theta_s = 135^\circ$ . The maximum reduction for  $C_D$  and r.m.s.  $C_L$  are 48% and 70%, respectively.

For the range of Reynolds number considered, drag on the cylinder is mostly attributed to the fore-aft pressure difference. The total drag can be written as the sum of a force arising from pressure difference,  $F_p$ , and total skin friction,  $F_v$ :  $F_D = F_p + F_v$ . Their relative contributions for  $Re=200$  and  $\beta=0.2$  are plotted in Fig. 9. Evidently pressure difference amounts to approximately 90% of the total drag in general. Figs. 9b and c demonstrate how  $F_p$  and  $F_v$  vary along with the slip azimuth,  $\theta_s$ , for the same Reynolds numbers and  $\beta$ . Both variables are normalized with their respective values at  $\theta_s = 0^\circ$ . While  $F_p$  reaches a minimum at  $\theta_s = 135^\circ$ , as expected, the effects on  $F_v$  saturates much earlier at  $\theta_s = 90^\circ$ . We remark that for the

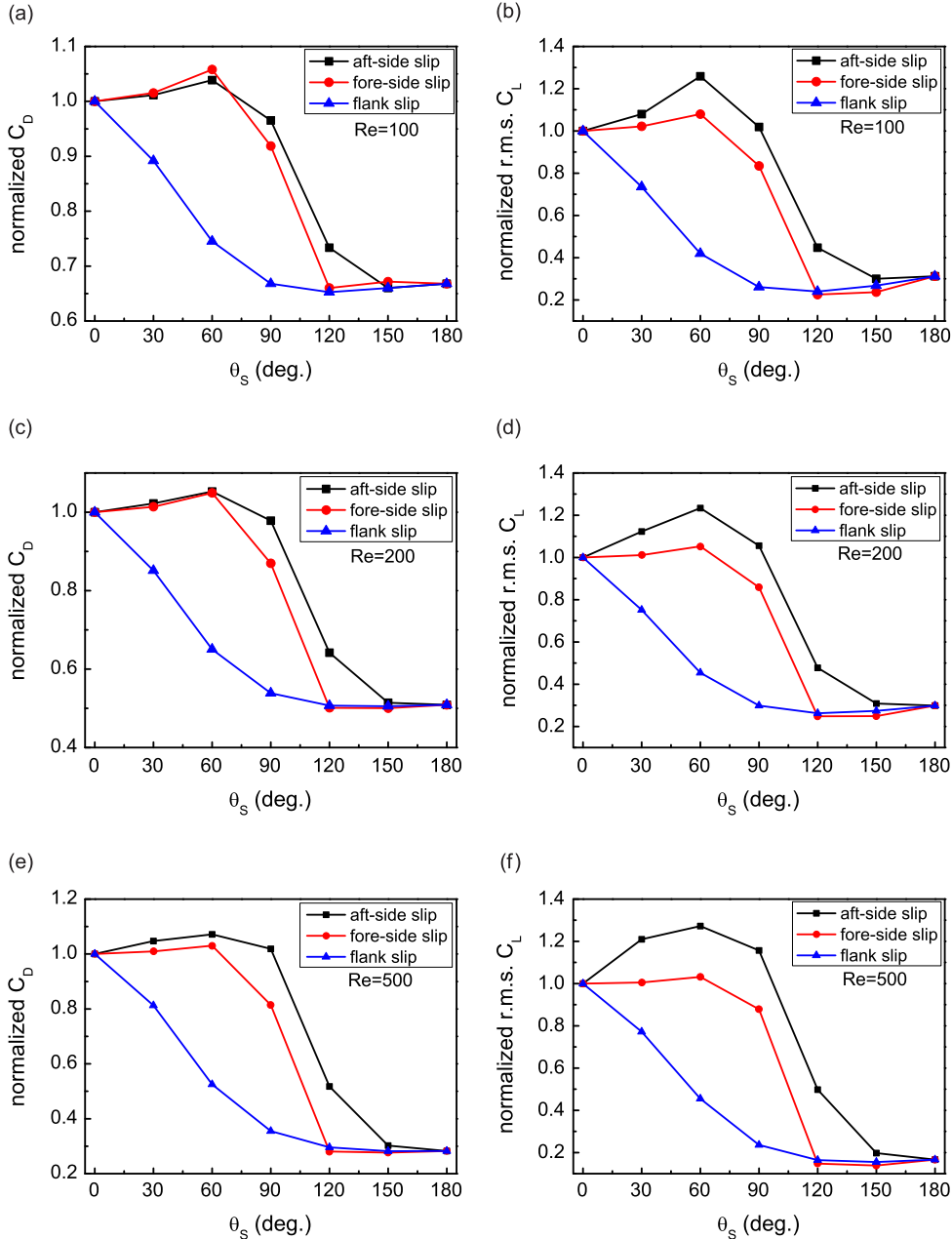


**Fig. 11.** The normalized drag coefficient and r.m.s. lift coefficient for the different distributed slip boundary conditions and  $Re=100, 200, 500$ : (a), (c), (e), the drag coefficient,  $C_D$ ; (b), (d), (f), the r.m.s. lift coefficient,  $C_L$ . For each case,  $\theta_s = 0^\circ$  and  $\theta_s = 180^\circ$  correspond to no slip and all slip, respectively. Flank slip is the most effective on drag and lift reduction.  $\beta=0.2$ .

cases studied above, where we only considered fore-side slip distribution, the change in the flow field, pressure, and drag and lift coefficients are only appreciable for  $\theta_s > 90^\circ$ . We speculate this trend is due to the fact that for  $\theta_s < 90^\circ$ , the separation locale cannot be effectively pushed back. However, on the other hand, having slip on the aft-semicircle alone cannot achieve the same effect as having fore-side slip with  $\theta_s > 90^\circ$ . (See further study below in Section 4.2.) This observation is an important insight provided by the current study.

Last but not least, we examine the Strouhal number which characterizes vortex shedding frequency. In Fig. 10, we show the normalized Strouhal number as a function of  $\theta_s$ . The shedding frequency increases with  $\theta_s$  when  $Re$  is less than 500, and asymptotes at  $\theta_s = 135^\circ$ . This trend is due to the fact that the rate-of-change for vorticity at the cylinder surface (which is proportional to  $St$ ) results from both diffusion through the boundary layer and advection along the cylindrical wall. The former is by-and-large unaffected by slip, whereas the strength of the latter increases linearly with the tangential velocity at the surface (Legendre et al., 2009), which in turn increases along with  $\theta_s$ .

#### 4.2. Comparison of different slip distribution types

In the previous subsection, we examined in detail the flow with fore-side slip distribution, and compared the results with no slip and all slip, which can be considered special cases for this configuration. In what follows, we study other distribution types, namely, flank slip and aft-side slip. These studies will help us establish strategies for slip placement for desired flow control effects. For brevity, we will only present the final results on the drag and lift coefficients. Figs. 11a,c,e shows the behavior of  $C_D$  for the three Reynolds numbers and slip distributions considered. For each graph,  $C_D$  is normalized with its value obtained with the no slip condition. Note that regardless of the slip type, the slip coverage is symmetric about the center axis along the flow direction, and the azimuth  $\theta_s$  indicates half of the total covered area (see Fig. 2). In addition,  $\theta_s = 0^\circ$  and  $180^\circ$  correspond to no slip and all slip, respectively. For fore-side slip, we have demonstrated previously that drag reduction is only noticeable for  $\theta_s > 90^\circ$ , and the effect saturates at about  $\theta_s = 135^\circ$ . Aft-side slip is the least effective.  $C_D$  even shows a slight increase for  $\theta_s < 90^\circ$ , and begins to decrease below 1 only after the coverage passes the apex toward the fore-side slip. In contrast, flank slip which is the symmetric upper and lower slip type is the most effective in drag

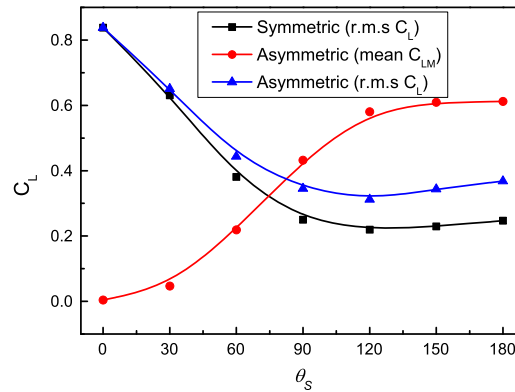


**Fig. 12.** The r.m.s lift force coefficient,  $C_L$ , and the mean lift coefficient,  $C_{LM}$ , as functions of  $\theta_s$  for flank slip. In the symmetric case,  $\beta$  equals 0.2 on both the upper and lower sides; in the asymmetric case,  $\beta$  equals 0.2 and 0.1 on the upper and lower sides, respectively.  $Re=200$ .

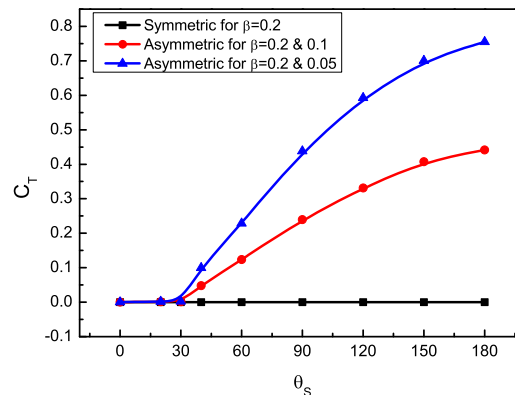


**Fig. 13.** The torque coefficients,  $C_T$ , as a function of  $\theta_s$  for flank slip. In the symmetric case,  $\beta$  equals 0.2 on both the upper and lower sides; in the asymmetric cases,  $\beta$  equals 0.2 on the upper side,  $\beta$  equals 0.1 and 0.05 on the lower side for two separate cases, respectively.  $Re=200$ .

reduction for comparable  $\theta_s$  values. For example, at  $\theta_s = 90^\circ$  for  $Re = 200$ , the  $C_D$  values are 0.87, 0.98, and 0.54 for fore-side slip, aft-side slip, and flank slip, respectively. For all slip types, the change in  $C_D$  is more evident when the Reynolds number increases within the laminar flow regime. In Figs. 11b,d,f, the trend for  $C_L$  is similar, with less difference across the Reynolds numbers. The above results establish that the flank of a cylinder is the best location to place slip boundaries should drag and lift reduction be desired. In other words, it suggests the area encompassing the apexes is the most essential in imparting impact on the flow field. Further study is needed to generalize this conclusion to other types of bluff body, or to flows with larger Reynolds numbers where turbulence is present.

Last but not least, we remark that should the slip distribution become asymmetric with respect to the center axis along the flow direction, non-zero lift force and torque generally ensue. To demonstrate these effects, different slip lengths asymmetrically distributed on the upper and lower sides for flank slip are studied. In Fig. 12, the r.m.s and mean lift forces are shown, for  $\beta$  equals 0.2 and 0.1 on the upper and lower sides, respectively, as functions of the distribution angle,  $\theta_s$ . A non-zero mean lift force is found to increase with  $\theta_s$ , reaching maximum at  $180^\circ$ . In general, the r.m.s lift force with an asymmetric slip distribution is greater than that with a symmetric slip distribution, which is also presented in Fig. 12 for reference. Fig. 13 shows the torque arising from asymmetric slip distribution. Two cases are studied, both with  $\beta$  equals 0.2 on the upper side, and 0.1 and 0.05 on the lower side, respectively. Evidently the torque in the symmetric case is not significant, whereas a larger asymmetry leads to a greater torque. For all distributions, the torque is not appreciable for  $\theta_s$  less than  $30^\circ$ .

## 5. Conclusions

In this work, we investigated the effects of slip distribution on flow past a circular cylinder. Both a theoretical analysis in the small-Reynolds-number regime and numerical simulations for moderate Reynolds numbers with various slip distribution types are presented. For the former, we have derived an asymptotic solution, and demonstrate that slip has only a higher order effect ( $\sim 1/\ln(Re)$ ) on the flow and pertinent parameters such as the drag coefficient. For moderate Reynolds numbers in the laminar flow regime, we have demonstrated that the implementation of slip boundaries are effective means to achieve flow control, through the alterations in the pressure field, the separation angle, and the wake structure. Furthermore, comparison of different slip distribution types reveals that the flanks of the cylinder is the best location to implement slip for drag and lift reduction. We also observe that rotation of the cylinder can be achieved by an asymmetric slip distribution. The current work contributes to the strategic planning of slip placement for bluff-body flow optimization.

## Acknowledgments

The following agencies and programs are acknowledged: Major State Basic Research Development Program of China (Grant no. 2011CB013101); National Natural Science Foundation of China (NSFC) under Grants 11225208, 11172001, and 11302006. Huiling Duan would like to acknowledge the Alexander von Humboldt (AvH) foundation (Germany) to support this work through the project “Mechanics theory of materials with complex surfaces and its applications”.

## Appendix A

Both grid types shown in Fig. 1 are tested for numerical convergence and accuracy. For the first type, which is used to validate the analytical solution in Section 2, we run the simulation with no slip boundary conditions at two Reynolds numbers,  $Re = 0.1$  and  $0.416$ . The thickness of the first row of cells,  $\delta$ , is chosen to be  $0.001D$  and  $0.005D$ . The resulting drag coefficient shown in Table A1 is compared against both experimental data (Tritton, 1959) and theoretical prediction:

$$C_D = \frac{1}{1 - \frac{1}{2}\gamma - \ln(Re/8)} \frac{8\pi}{Re}. \quad (A.1)$$

Satisfactory numerical convergence and accuracy are achieved at  $\delta = 0.005D$ .

Similarly, the second grid type shown in Fig. 1 is tested against both numerical simulations (Legendre et al., 2009; Persillon and Braza, 1988; Karniadakis and Triantafyllou, 1989) and experimental data (Williamson, 1988), and the comparison is summarized in Table A2. For all cases no-slip boundary conditions are prescribed.

**Table A1**

Comparison of drag coefficient (with no slip boundary condition) from experimental data, theoretical prediction, and the current simulation.

Re	0.1	0.416
Experimental Tritton, 1959	57.5	18.6
Theoretical (A.15)	58.4	20.98
Numerical	$\delta = 0.001D$	59.3
	$\delta = 0.005D$	59.6
		19.3

**Table A2**

Comparison of the drag coefficient ( $C_D$ ), lift coefficient ( $C_L$ ), and Strouhal number ( $St$ ) obtained from the current simulation with previous numerical results and experimental data.

Re	100	200	500
$C_D$			
Ref. Legendre et al., 2009, 2D (3D)	1.253 (1.240)	1.321 (1.306)	
Ref. Persillon and Braza, 1988, 2D	1.350	1.345	1.379
Current, 2D	1.356	1.349	1.434
$C_L$			
Ref. Legendre et al., 2009, 2D (3D)	0.39 (0.36)	0.76 (0.64)	
Ref. Persillon and Braza, 1988, 2D	0.334	0.70	1.11
Current, 2D	0.242	0.494	0.834
$St$			
Ref. Legendre et al., 2009, 2D (3D)	0.165 (0.164)	0.198 (0.181)	
Ref. Persillon and Braza, 1988, 2D	0.176	0.204	0.222
Ref. Karniadakis and Triantafyllou, 1989, 2D	0.179	0.206	
Current, 2D	0.162	0.196	0.227
Ref. Williamson, 1988, experimental	0.164	0.197	

## Appendix B

We search for a solution expanded with respect to  $1/\Delta(\text{Re})$ . The leading term of the outer region is  $\psi_0 = \sigma \sin \theta$ . The flow region near the surface of cylinder satisfies the Stokes approximation, and Eq. (6) becomes

$$\nabla_r^4 \phi_1 = 0. \quad (\text{B.1})$$

The general solution for Eq. (B.1) is

$$\phi_1 = \left( c_{11}r^3 + c_{12}r \ln r + c_{13}r + \frac{c_{14}}{r} \right) \sin \theta + \sum_{n=2}^{\infty} (c_{n1}r^{n+2} + c_{n2}r^n + c_{13}r^{-n+2} + c_{14}r^{-n}) \sin n\theta, \quad (\text{B.2})$$

where  $c_{n1}, c_{n2}, c_{n3}, c_{n4}$  are constants. Considering the boundary condition (7) and changing the variable from  $r$  to  $\sigma$  to match the leading term of the far field, we obtain

$$\phi_1 = -\frac{1}{\Delta(\text{Re}_a)} \left[ r \ln r + \frac{1}{2(1+2\beta)} \left( \frac{1}{r} - r \right) \right] \sin \theta. \quad (\text{B.3})$$

Because we do not change the governing equation of the stream function (B.1), the form of stream function  $\phi$  is similar to  $\phi_1$ . We may then assume

$$\phi = -\left[ \frac{1}{\Delta(\text{Re}_a)} + \frac{\alpha_2}{\Delta^2 \text{Re}_a} \right] \left[ r \ln r + \frac{1}{2(1+2\beta)} \left( \frac{1}{r} - r \right) \right] \sin \theta. \quad (\text{B.4})$$

We can subsequently use the Oseen equation to obtain  $\psi_1$ . Eq. (6) becomes

$$\begin{cases} \left( \nabla_\sigma^2 - \frac{\partial}{\partial \xi} \right) \nabla_\sigma^2 \psi_1 = 0, \\ \xi = \sigma \cos \theta. \end{cases} \quad (\text{B.5})$$

The boundary condition Eq. (7) is

$$\lim_{\sigma \rightarrow \infty} (\sigma \sin \theta + \sum_{n=1}^{\infty} F_n \psi_n) = \sigma \sin \theta. \quad (\text{B.6})$$

We therefore obtain

$$\lim_{\sigma \rightarrow \infty} \psi_1 = 0. \quad (\text{B.7})$$

We arrive at

$$\nabla_\sigma^2 \psi_1 = e^{\frac{1}{2}\xi} \sum_{n=1}^{\infty} X_n K_n \left( \frac{1}{2}\sigma \right) \sin n\theta, \quad (\text{B.8})$$

where  $X_n$ 's are constants and  $K_n$  are the modified Bessel functions. The matching condition between infield and outfield is

$$\nabla_\sigma^2 \psi = \frac{1}{\text{Re}} \nabla_r^2 \phi, \quad (\text{B.9})$$

so we can obtain

$$\nabla_\sigma^2 \psi_1 = -e^{\frac{1}{2}\xi} K_1 \left( \frac{1}{2}\sigma \right) \sin \theta, \quad (\text{B.10})$$

and

$$F_1(\text{Re}_a) = \frac{1}{\Delta(\text{Re}_a)}. \quad (\text{B.11})$$

Finally, we obtain  $\psi_1$

$$\psi_1 = \sum_{n=1}^{\infty} \varphi_n \left( \frac{1}{2} \sigma \right) \frac{\sigma \sin n\theta}{n}, \quad \varphi_n = 2K_1 I_n + K_0(I_{n-1} + I_{n+1}). \quad (\text{B.12})$$

where  $K_n$  and  $I_n$  are the modified Bessel functions. Next we compute  $\psi_2$ . The governing equation is

$$\left( \nabla_{\sigma}^2 - \frac{\partial}{\partial \xi} \right) \nabla_{\sigma}^2 \psi_2 = -\frac{1}{\sigma} \frac{\partial(\psi_1, \nabla_{\sigma}^2 \psi_1)}{\partial(\sigma, \theta)}. \quad (\text{B.13})$$

Consider Eq. (B.12) and get

$$-\frac{1}{\sigma} \frac{\partial(\psi_1, \nabla_{\sigma}^2 \psi_1)}{\partial(\sigma, \theta)} = e^{\frac{1}{2}\xi} \sum_{n=1}^{\infty} g_n(\sigma) \sin n\theta, \quad (\text{B.14})$$

where  $g_1 \sim \text{Re}_a^{-1}$ ,  $g_2 \sim \text{Re}_a^{-2}$ , and  $g_p \sim \text{Re}_a^{p-2}$  ( $p > 2$ ). The boundary condition is the same as  $\psi_1$ , namely,  $\lim_{\sigma \rightarrow \infty} \psi_2 = 0$ . We obtain

$$\nabla_{\sigma}^2 \psi_2 = \sum_{n=1}^{\infty} k_n(\sigma) \sin n\theta + e^{\frac{1}{2}\xi} \sum_{n=1}^{\infty} Z_n K_n \left( \frac{1}{2} \sigma \right) \sin n\theta, \quad (\text{B.15})$$

and

$$F_2(\text{Re}_a) = \frac{1}{\Delta^2(\text{Re}_a)}. \quad (\text{B.16})$$

$\psi_2$  is then solved to be

$$\psi_2 = -\alpha_2 \sum_{n=1}^{\infty} \varphi_n \left( \frac{1}{2} \sigma \right) \frac{\sigma \sin n\theta}{n} + \sum_{n=1}^{\infty} l_n(\sigma) \sin n\theta, \quad (\text{B.17})$$

where  $X_n$  and  $K_n$  are the modified Bessel functions, and  $l_n(\text{Re}_a) \sim \text{Re}_a^n$ . Consider the  $O(1/\Delta(\text{Re}_a))$  term of  $\psi$  in the far-field and comparing it with the solution near the surface, we arrive at  $\alpha_2 = 0$ . Then we obtain a solution near the surface of the cylinder:

$$\phi = -\frac{1}{\Delta(\text{Re}_a)} \left[ r \ln r + \frac{1}{2(1+2\beta)} \left( \frac{1}{r} - r \right) \right] \sin \theta. \quad (\text{B.18})$$

Equation (B.18) is valid when  $\text{Re}_a r \ln r \ll 1$ ; that is, when viscous effects dominate.

## References

- Breuer, M., 2000. A challenging test case for large eddy simulation high reynolds number circular cylinder flow. *International Journal of Heat and Fluid Flow* 21, 648–654.
- Choi, H., Moin, P., Kim, J., 1994. Active turbulence control for drag reduction in wall-bounded flows. *Journal of Fluid Mechanics* 262, 75–110.
- Daniello, R., Muralidhar, P., Carron, N., Greene, M., Rothstein, J.P., 2013. Influence of slip on vortex-induced motion of a superhydrophobic cylinder. *Journal of Fluids and Structures* 42, 358–368.
- Deng, R., Wang, C.H., Smith, K.A., 2006. Bubble behavior in a Taylor vortex. *Physical Review E* 73 (3), 036306.
- Fish, F.E., Lauder, G.V., 2006. Passive and active flow control by swimming fishes and mammals. *Annual Review of Fluid Mechanics* 38, 193–224.
- Fluent6.1, User's Guide.
- Gillies, E.A., 1998. Low-dimensional control of the circular cylinder wake. *Journal of Fluid Mechanics* 371, 157–178.
- Hanchi, S., Askovic, R., Phuoc, L.T., 1999. Numerical simulation of a flow around an impulsively started radially deforming circular cylinder. *International Journal for Numerical Methods in Fluids* 29, 555–573.
- Hendy, S.C., Lund, N.J., 2007. Effective slip boundary conditions for flows over nanoscale chemical heterogeneities. *Physical Review E* 76 (6), 066313.
- Joseph, P., Tabeling, P., 2005. Direct measurement of the apparent slip length. *Physical Review E* 71 (3), 035303.
- Kaplun, S., 1957. Low Reynolds number flow past a circular cylinder. *Journal of Mathematics and Mechanics* 6 (5), 52–60.
- Karniadakis, G.E., Triantafyllou, G.S., 1989. Frequency selection and asymptotic states in laminar wakes. *Journal of Fluid Mechanics* 199, 441–469.
- Lagerstrom, P.A., Cole, J., 1955. Examples illustrating expansion procedures for the Navier–Stokes equations. *Journal of Rational Mechanics and Analysis* 4, 817–882.
- Lamb, H., 1911. XV. On the uniform motion of a sphere through a viscous fluid. *Philosophical Magazine Series* 6 21 (121), 112–121.
- Lauga, E., Brenner, M.P., Stone, H.A., 2007. *Microfluidics: The No-Slip Boundary Condition*, Handbook of Experimental Fluid Dynamics. Springer.
- Lee, C., Kim, C.J.C.J., 2009. Maximizing the giant liquid slip on superhydrophobic microstructures by nanostructuring their sidewalls. *Langmuir* 25 (21), 12812–12818.
- Legendre, D., Lauga, E., Magnaudet, J., 2009. Influence of slip on the dynamics of two-dimensional wakes. *Journal of Fluid Mechanics* 633, 437.
- Lund, N.J., Zhang, X.P., Mahelona, K., Hendy, S.C., 2012. Calculation of effective slip on rough chemically heterogeneous surfaces using a homogenization approach. *Physical Review E* 86 (4), 046303.
- Mittal, S., Kumar, B., 2003. Flow past a rotating cylinder. *Journal of Fluid Mechanics* 476 (4), 303–334.
- Muralidhar, P., Ferrer, N., Daniello, R., Rothstein, J.P., 2011. Influence of slip on the flow past superhydrophobic circular cylinders. *Journal of Fluid Mechanics* 680, 459–476.
- Ou, J., Moss, G.R., Rothstein, J.P., 2007. Enhanced mixing in laminar flows using ultrahydrophobic surfaces. *Physical Review E* 76, 016304, <http://dx.doi.org/10.1103/PhysRevE.76.016304>.

- Ozono, S., 1999. Flow control of vortex shedding by a short splitter plate asymmetrically arranged downstream of a cylinder. *Physics of Fluids* 11 (10), 2928.
- Padrino, J.C., Joseph, D.D., 2006. Numerical study of the steady-state uniform flow past a rotating cylinder. *Journal of Fluid Mechanics* 557, 191.
- Patankar, S.V., 1980. *Numerical Heat Transfer and Fluid Flow*. Taylor & Francis.
- Persillon, H., Braza, M., 1988. Physical analysis of the transition to turbulence in the wake of a circular cylinder by three-dimensional Navier–Stokes simulation. *Journal of Fluid Mechanics* 365, 23–88.
- Priezjev, N.V., Darhuber, A.A., Troian, S.M., 2005. Slip behavior in liquid films on surfaces of patterned wettability: comparison between continuum and molecular dynamics simulations. *Physical Review E* 71 (4), 041608.
- Proudman, I., Pearson, J.R.A., 1957. Expansions at small Reynolds numbers for the flow past a sphere and a circular cylinder. *Journal of Fluid Mechanics* 2, 237–262. <http://dx.doi.org/10.1017/S0022112057000105>.
- Quéré, D., 2005. Non sticking drops. *Reports on Progress in Physics* 68 (11), 2495–2532.
- Reichl, P., Hourigan, K., Thompson, M.C., 2005. Flow past a cylinder close to a free surface. *Journal of Fluid Mechanics* (2005) 533.
- Rothstein, J.P., 2010. Slip on superhydrophobic surfaces. *Annual Review of Fluid Mechanics* 42 (1), 89–109.
- Sirovich, L., Karlsson, S., 1997. Turbulent drag reduction by passive mechanisms. *Nature* 388 (1997) 753–755.
- Strouhal, V., 1878. Ueber eine besondere Art der Tonerregung. *Annalen der Physik* 241 (10), 216–251.
- Swan, J.W., Khair, A.S., 2008. On the hydrodynamics of ‘slip–stick’ spheres. *Journal of Fluid Mechanics* (2008) 606.
- Thalakkottor, J.J., Mohseni, K., 2013. Analysis of boundary slip in a flow with an oscillating wall. *Physical Review E* 87 (3), 033018.
- Tritton, D.J., 1959. Experiments on the flow past a circular cylinder at low Reynolds numbers. *Journal of Fluid Mechanics* 6 (4), 547–567.
- Vakarelski, I.U., Patankar, N.A., Marston, J.O., Chan, D.Y.C., Thoroddsen, S.T., 2012. Stabilization of leidenfrost vapour layer by textured superhydrophobic surfaces. *Nature* 489 (7415), 274–277.
- Williamson, C.H.K., 1988. Defining a universal and continuous Strouhal–Reynolds number relationship for the laminar vortex shedding of a circular cylinder. *Physics of Fluids* 31 (10), 2742.
- Wu, M.H., Wen, C.Y., Yen, R.H., Weng, M.C., Wang, A.B., 2004. Experimental and numerical study of the separation angle for flow around a circular cylinder at low Reynolds number. *Journal of Fluid Mechanics* 515, 233–260.
- Xue, Y., Chu, S., Lv, P., Duan, H., 2012. Importance of hierarchical structures in wetting stability on submersed superhydrophobic surfaces. *Langmuir* 28 (25), 9440–9450.
- You, D., Moin, P., 2007. Effects of hydrophobic surfaces on the drag and lift of a circular cylinder. *Physics of Fluids* 19 (8), 081701.